Magnetic linear dichroism in valence-band photoemission: Experimental and theoretical study of Fe(110)

A. Rampe and G. Güntherodt
2. Physikalisches Institut, Rheinisch-Westfälische Technische Hochschule Aachen, D-52056 Aachen, Germany

D. Hartmann
Siemens AG, Hofmannstr. 51, D-81359 München, Germany

J. Henk
Condensed Matter Theory Group, Physics Department, Uppsala University, S-751 21 Uppsala, Sweden

T. Scheunemann and R. Feder
Theoretische Festkörperphysik, Universität Duisburg, D-47048 Duisburg, Germany
(Received 10 September 1997; revised manuscript received 14 January 1998)

Magnetic linear dichroism (MLD) in angle-resolved valence-band photoemission of Fe(110) has been investigated by means of symmetry considerations, analytical theory, numerical calculations, and photoemission measurements. The dichroic photoemission spectra and their dependence on photon energy clearly show that the microscopic origin of MLD is an interference effect induced by hybridization of initial states of different spatial symmetry at band gaps arising from spin-orbit coupling. The dependence of MLD on the light incidence angle evidences that it is substantially influenced by the optical response of the metal, the approximation of which according to classical Fresnel theory is adequate to reproduce our experimental data.
[S0163-1829(98)04618-9]

I. INTRODUCTION

Spin-orbit coupling (SOC) in the valence bands is the microscopic origin of magnetic phenomena such as the magneto-optical Kerr effect and the magnetocrystalline anisotropy. However, up to the present it has not been clarified in detail how SOC influences these effects. For example, the question arises which electronic states are responsible for a large Kerr rotation or determine the direction of the easy axis of the magnetization. In principle, the mechanism is well understood: starting from the spin-polarized band structure of a ferromagnet, SOC further reduces the symmetry of the system. Hybridization between spin-up and spin-down bands occurs and degeneracies between them are removed. Consequently, the energy levels depend on the magnetization direction and total-energy calculations yield the easy axis. Therefore, it is of general interest to have a wide basis of experimental and theoretical data in order to answer in detail the question of how SOC influences the electronic structure.

In the last few years it has experimentally[1–6] and theoretically[7–15] been shown that SOC is a necessary ingredient for the various types of magnetic dichroism. Under the term magnetic dichroism those phenomena are collected where an observable, e.g., the x-ray absorption coefficient or the photoemission intensity, depends on the magnetization direction (for reviews on SOC-influenced spectroscopies we refer to Ref. 16). One of these dichroism effects is magnetic linear dichroism (MLD) in the angular distribution of photoelectrons. It commonly denotes the dependence of the angle-resolved photoemission intensity under excitation by linearly polarized light on magnetization reversal. Due to the close connection of SOC-induced spin polarization to dichroism, the relativistic electronic structure has been successfully investigated by magnetic circular dichroism for Ni(100).[17] How MLD can be used to study in detail relativistic band structures will be shown in this paper.

In this joint experimental and theoretical study we focus on MLD in the valence-band photoemission from Fe(110). Our investigations rely on an analytical theory,[12] the application of which to Fe(110) is presented in Sec. III A. It allows us to show, in Sec. IV C, that the microscopic origin of the actually observed MLD is a SOC-induced hybridization between wave functions with spatial Σ^1 and Σ^3 symmetry. To make more quantitative contact with the experimental data, we performed numerical calculations using a spin-polarized relativistic layer Korringa-Kohn-Rostoker (KKR) formalism. The comparison of experiment, numerical calculations, and analytical theory in Sec. IV provides a consistent picture and in particular evidences the adequacy of our theoretical methods. Additionally, it reveals how the MLD for *p*-polarized light is modified by the optical response of the solid.

MLD by itself is an interference effect, so it is very sensitive, for example, to SOC (Ref. 19) and to the magnetization. Founded upon this result, we discuss in which way MLD can be used to obtain detailed information on the relativistic valence-band structure or other magnetic properties, e.g., the arrangement of magnetic moments.[20]

II. EXPERIMENTAL ASPECTS

Experimental spectra were recorded at the monochromator beam line TGM3 of the synchrotron radiation facility BESSY, Berlin. It provides photons in the energy range from

14 to 30 eV and from 30 to 70 eV with two different gratings. The degree of linear polarization of the light decreases monotonously over the whole photon energy range from 90% at 15 eV down to 70% at 70 eV. The kinetic-energy analysis of the photoelectrons was performed by an 180° hemispherical analyzer with 50 mm diameter and an angular resolution of $\pm 2°$. The combined energy resolution of photons and electrons was 200 meV. Additionally, the photon flux has continuously been recorded during the measurements in order to normalize the spectra. The geometrical setup is described in Sec. III A.

Ferromagnetic Fe layers were grown *in situ* on a W(110) single crystal in an UHV chamber with base pressure of 5×10^{-11} mbar, which increases during electron-beam evaporation to 1×10^{-10} mbar. The bulklike, 15 atomic layer (AL) thick Fe layers were evaporated at a rate of 0.5 AL/min and at a substrate temperature of 450 K. The layer thickness was measured during the evaporation with a calibrated quartz microbalance with an accuracy of $\pm 5\%$.

These preparation conditions result in sharp low-energy electron-diffraction (LEED) spots with a low background evidencing the epitaxial growth of the Fe layers on the bcc W(110) substrate. Three growth phases can be distinguished. During all phases the symmetry of the LEED pattern is $2mm(C_{2v})$. The first two monolayers grow pseudomorphically, i.e., the LEED pattern of the Fe and the clean W substrate are identical. For thicknesses between 2 AL and 10 AL one observes a superstructure in the LEED patterns caused by periodic lattice distortions compensating the lattice misfit of 9.4% between Fe and W. Above 10 AL Fe the distortion-induced superstructure is no longer visible in LEED and one observes the LEED pattern of a clean bcc(110) surface. The distance between the spots and intensity vs energy curves evidence that the film grows now with the lattice constant of bulk bcc Fe. In addition, growth and cleanliness have been checked with Auger electron spectroscopy. Distinct kinks for each completed monolayer in the intensity of the 47 eV Auger line as a function of Fe thickness evidence layer-by-layer growth up to 3 AL. Further details of the preparation have been published elsewhere.[21]

III. THEORETICAL ASPECTS

A. Analytical results

In this section we discuss briefly the microscopic origin of MLD by means of symmetry considerations and analytical calculations, both applied to our specific setup (cf. Fig. 1). For the MLD the Fe(110) film is remanently magnetized along the two in-plane easy axes, i.e., in the [110] and [$\bar{1}$10] direction ($\pm y$ axis) and the magnetization reads $\vec{M}_{\pm} = (0, \pm M, 0)$. P-polarized light impinges under a polar angle ϑ on the surface. We distinguish two light polarizations $p_{\pm}$ with electric-field vectors $\vec{E}(p_{\pm}) = E_0(\pm \cos\vartheta, 0, \sin\vartheta)$. The electrons are detected along the surface normal ([110], z axis).

As mentioned above, the point group of a cubic (110) surface of a nonmagnetic solid, $2mm(C_{2v})$, has four symmetry operations: the identity E, the twofold rotation about the surface normal C_2, the reflection at the (x,z) plane m_y, and the reflection at the (y,z) plane m_x. Its single group has four

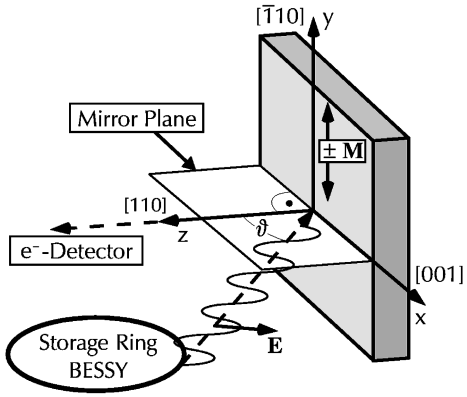

FIG. 1. Standard setup for magnetic linear dichroism in photoemission from cubic (110) surfaces. The crystal is remanently magnetized along the [$\bar{1}$10] ($\vec{M}_+$) or the [1$\bar{1}$0] ($\vec{M}_-$) direction. P-polarized light impinges at a polar angle ϑ onto the surface. Its electric field vector $\vec{E}$ lies within the mirror plane that is perpendicular to $\vec{M}$ and contains the surface normal. Photoelectrons are detected in normal emission.

one-dimensional irreducible representations, $\Sigma^s, s = 1, \ldots, 4$, its double group a single two-dimensional irreducible representation, Σ_5. The presence of the magnetization $\vec{M}$ reduces the symmetry to point group m, with symmetry operations E and m_y. Its double group has two one-dimensional irreducible representations, γ_+ and γ_-, which are degenerate by time reversal.[22,23] Already at this point, symmetry considerations show that MLD should exist (cf. Table I). The operations of $2mm$ leave $(p_+, \vec{M}_+)$ either invariant or turn it into $(p_-, \vec{M}_-)$. In other words, there is no operation that reverses $\vec{M}$ and simultaneously leaves the light polarization invariant: there is MLD. The operation m_y gives for the components of the photoelectron spin polarization $P_x = P_z = 0$ and $P_y \neq 0$. The latter component is already present in the nonmagnetic case due to the linear spin-polarization effect (LSPE) by Tamura and Feder[24,25] (discussed below). For normal incidence [$\vartheta = 0°$, $\vec{E}(p_+) = -\vec{E}(p_-)$] or grazing incidence [$\vartheta = 90°$, $\vec{E}(p_+) = \vec{E}(p_-)$], there is no MLD (cf. operation m_x).

To elucidate the origin of the MLD in detail, we decompose the electronic states of the semi-infinite system into wave functions $|R^s_{\pm} \Sigma^s \tau^s\rangle$. The spin τ^s is described by Pauli spinors $|\alpha\rangle$ and $|\beta\rangle$ quantized along the magnetization direction. The angular parts belonging to Σ^s, with $s = 1, \ldots, 4$ consist of symmetry-adapted combinations of spherical harmonics. Collecting the various parts, each electronic state $\Psi_{\pm}$ belonging to $\gamma_{\pm}$ can be written as

TABLE I. Effect of symmetry operations of the point group $2mm$ on light polarization p_+, magnetization $\vec{M}_+$, and photoelectron spin polarization $\vec{P} = (P_x, P_y, P_z)$.

E:	p_+	$\vec{M}_+$	$+P_x$	$+P_y$	$+P_z$
C_2:	p_-	$\vec{M}_-$	$-P_x$	$-P_y$	$+P_z$
m_x:	p_-	$\vec{M}_-$	$+P_x$	$-P_y$	$-P_z$
m_y:	p_+	$\vec{M}_+$	$-P_x$	$+P_y$	$-P_z$

$$|\Psi_+\rangle = |R_+^1 \Sigma^1 \alpha\rangle + |R_+^3 \Sigma^3 \alpha\rangle + |R_+^2 \Sigma^2 \beta\rangle + |R_+^4 \Sigma^4 \beta\rangle, \tag{1a}$$

$$|\Psi_-\rangle = |R_-^1 \Sigma^1 \beta\rangle + |R_-^3 \Sigma^3 \beta\rangle + |R_-^2 \Sigma^2 \alpha\rangle + |R_-^4 \Sigma^4 \alpha\rangle. \tag{1b}$$

The superscript s on the radial parts $R_\pm^s$ refers to the single-group representation Σ^s. Their subscripts are not to be confused with a spin index: each state contains both Pauli spinors due to SOC. In the nonmagnetic case, Kramers' degeneracy requires $R_+^s = R_-^s, s = 1, \ldots, 4$. Since in the magnetic case Kramers' degeneracy is lifted, one member of a pair of exchange-split electronic states belongs to γ_+, the other to γ_-, and we have $R_+^s \neq R_-^s$.

We now sketch the analytical calculation of the photoemission intensity I (for details, see Ref. 12). Initial states are given by Eq. (1). Final states are mainly of Σ^1 spatial symmetry[26] due to the absence of exchange and SOC in the vacuum. In fact, SOC leads to scattering into wave-function parts with other spatial symmetries. However, the dominant component is of Σ^1 spatial symmetry. We therefore approximate the final-state wave function by regarding only the latter component. The transition-matrix elements $M^{(sfi)}$ are indicated by the single-group representation ($\Sigma^s, s = 1, \ldots, 4$) of the respective radial-angular part of the initial state, the double-group representation γ_i ($i = \pm$) of the initial state, and γ_f ($f = \pm$) of the final state. The radiation field inside the solid is approximated macroscopically according to classical electrodynamics[27] (Snell's law and Fresnel's formula) that leads to significant effects on the photoelectron spin polarization and on magnetic dichroism (for details see Refs. 18 and 28). We denote internal quantities (field vector E_0' and propagation angle ϑ') of the light by a prime. In dipole approximation, selection rules yield: (i) E_{0x}' induces transitions from Σ^3 components of the initial states, the corresponding matrix elements being $E_0' \cos\vartheta' M^{(3fi)}$. (ii) E_{0z}' connects initial- and final-state functions both with Σ^1 spatial symmetry and matrix elements $E_0' \sin\vartheta' M^{(1fi)}$. (iii) In our setup, Σ^2 and Σ^4 components of the initial states cannot be observed. (iv) Spin conservation within the excitation process requests $f = i$ for the matrix elements $M^{(1fi)}$ and $M^{(3fi)}$.

These selection rules in conjunction with the formation of SOC-induced hybrids have two important consequences. (i) Each initial state with an admixture of Σ^1 or Σ^3 functions can be observed; i.e., also a band with nonrelativistic Σ^2 or Σ^4 symmetry can contribute to the photoemission intensity. (ii) Initial states with simultaneously nonzero Σ^1 and Σ^3 parts have the same final state in the excitation process. Hence, there is interference between the Σ^1- and Σ^3-related transitions.

From the photoemission intensities $I(M_\pm)$ for the two magnetization directions,[12] we define the difference $D^{\mathrm{MLD}} = [I(\vec{M}_+) - I(\vec{M}_-)]/2$ and the sum $S^{\mathrm{MLD}} = [I(\vec{M}_+) + I(\vec{M}_-)]/2$. The resulting expressions are

$$D^{\mathrm{MLD}}(\vartheta') = 2|E_0'|^2 \mathrm{Im}[\sin\vartheta' \cos\vartheta' * (M^{(1++)} * M^{(3++)} - M^{(1--)\star} M^{(3--)})], \tag{2a}$$

$$S^{\mathrm{MLD}}(\vartheta') = |\sin\vartheta' E_0'|^2 (|M^{(1++)}|^2 + |M^{(1--)}|^2) + |\cos\vartheta' E_0'|^2 (|M^{(3++)}|^2 + |M^{(3--)}|^2), \tag{2b}$$

with initial states $|\Psi_+\rangle$ and $|\Psi_-\rangle$ at the same initial-state energy E_i. [The energy- and $\vec{k}_\parallel$-conserving terms $\delta(E_\mathrm{f} - E_\mathrm{i} - h\nu) \times \delta(\vec{k}_\parallel)$ have been omitted for clarity. The asterisk denotes the complex conjugation.] Reversal of the magnetization turns $M^{(sfi)}$ into $M^{(s,-f,-i)}$, which changes the sign of D^{MLD}, whereas S^{MLD} is invariant. Without SOC there would be no products of matrix elements with different spatial index i that leads to a vanishing D^{MLD}. In the nonmagnetic limit, the matrix elements $M^{(sfi)}$ and $M^{(s,-f,-i)}$ become equal and there is obviously no MLD. At last, the MLD vanishes also, in accordance with symmetry arguments, for normal incidence ($\vartheta = 0°$) and grazing incidence ($\vartheta = 90°$) because in these cases only one hybrid component is excited.

The origin of MLD in standard geometry can be attributed to the LSPE for p-polarized light.[24,25,29] In the nonmagnetic limit, the ''surviving'' term in the expression for P_y (not shown here) is an interference term that in this case is exclusively due to SOC, i.e., it is due to the LSPE. Furthermore, this LSPE can be regarded as the origin of MLD, because the corresponding transition-matrix elements are involved in the interference terms in both the intensity and spin-polarization expressions.[30]

Collecting Snell's law, Fresnel's formula, and Eq. (2), a rather complicated dependence of S^{MLD} and D^{MLD} on the incidence angle ϑ is obtained. Approximating the internal field by the external one, D^{MLD} shows a $\sin 2\vartheta$ dependence and S^{MLD} can be written as $A\sin^2\vartheta + B\cos^2\vartheta$, with $A(B)$ comprising the terms with the $M^{(1fi)}(M^{(3fi)})$ matrix elements. Note, within this approximation, S^{MLD} is extremal at normal or grazing incidence, whereas D^{MLD} is extremal at 45°.

In summary, our model of MLD is based on four ingredients: (i) SOC induces the formation of hybrids consisting of wave functions with different spatial-spin symmetry. (ii) The simultaneous excitation of partial waves from the different hybrid components results in an interference term in the photoemission intensity. (iii) This additional contribution to the photocurrent is spin polarized and changes sign, if the magnetization is reversed, i.e., MLD is observed. (iv) The optical response of the solid has been incorporated by taking the macroscopic classical electrodynamics into account.

B. Computational method

Numerical calculations of band structures, of layer-resolved densities of states (DOS), and of photoemission intensities have been performed within the framework of the spin-polarized relativistic layer KKR method.[31,32] Instead of

the bcc Fe film of 15 AL finite thickness used in the experiment, we take semi-infinite bcc Fe(110) with bulk lattice constant $a=2.87$ Å. This approximation is justified since first, due to the small escape depth of the photoelectrons, emission from the actual W substrate is negligible, and second, quantum-well states are not resolved in the present experiment. The surface geometry is not relaxed, as one expects for a closed packed surface and as has been determined by LEED for Fe(110).[33]

The effective spin-dependent muffin-tin potential has been obtained by a self-consistent bulk linear muffin-tin orbital (LMTO) calculation, but modified in some respects. First, the real part of the inner potential (10.5 eV with reference to E_F) has, for the occupied states, been augmented by a self-energy correction term $0.1(E-E_F)$ in order to reproduce the measured quasiparticle exchange splitting. Second, the spin-dependent potential in the topmost layer has been linearly rescaled[34] such as to achieve a magnetic moment enhanced by 20% relative to that in the bulk.[33–35]

The surface-potential barrier has been approximated by a reflecting step function $0.48a$ above the outermost internuclear plane. This simple model is adequate for the present purpose, since it yields a layer-resolved DOS almost identical with the one from a self-consistent surface LMTO calculation.

In our photoemission calculations, lifetime effects are incorporated by an energy-dependent imaginary part of the inner potential V_i. For the lower states (holes) we use $V_i=-0.2(E_F-E+0.25$ eV) and for the upper states $V_i=-0.05(E-E_F)$. V_i leads to broadening and shifts of peaks to lower binding energy with respect to the real-potential band structure. The radiation field inside the metal has been taken into account according to classical optics (Snell's and Fresnel's formulas).[18,28]

IV. RESULTS AND DISCUSSION

Since our photoemission spectra and their MLD can be interpreted in terms of direct bulk interband transitions, we first focus on the relativistic band structure. Subsequently, measured and calculated photoemission spectra are presented, and the microscopic origin of the MLD is discussed. Finally, the dependence of the MLD on the incidence angle of the photons is shown.

A. Band structure

Figure 2 shows the relativistic band structure of ferromagnetic Fe along the $\Gamma-\Sigma-N$ direction, the relevant one in normal emission geometry from the bcc(110) surface. For its calculation we used the bulk part of the potential as specified in Sec. III B, except that the imaginary part of the optical potential for the lower states has been set to zero, which yields so-called real bands. The bands are classified according to their double-group representation, γ_+ and γ_-. In addition, the dominant spatial-spin representation is indicated. This usual nonrelativistic characterization is a good approximation over large parts of the bands, but of course breaks down at SOC-induced band gaps due to the high degree of hybridization.

Four of these particularly interesting regions, in which Σ^1 and Σ^3 states are strongly hybridized, are marked in Fig. 2 by circles *A* to *D*. Circles *A* and *B* belong to the band gaps at the ''nonrelativistic'' points $\Gamma^{25'}\uparrow$ and $\Gamma^{25'}\downarrow$, respectively. At *C* (left panel) the situation is more complicated; three band gaps occur in this region, the largest one between the $\Sigma^1\uparrow$ and the $\Sigma^3\uparrow$ band. The anticrossing point *D* between $\Sigma^1\downarrow$ and $\Sigma^3\downarrow$ belongs to the unoccupied states.

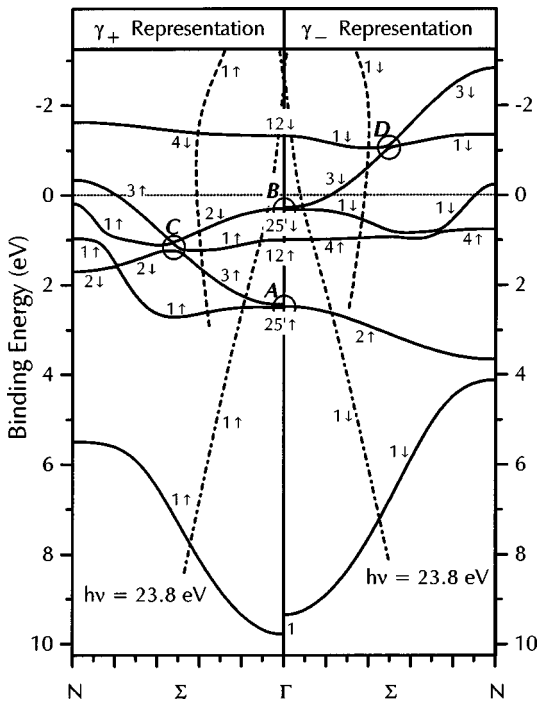

FIG. 2. Relativistic valence band structure of Fe(110) separated into representations γ_+ (left panel) and γ_- (right panel) of double group *m*. Labels indicate the spatial-spin symmetry of the dominating component of the respective initial state. Circles denote SOC-induced band gaps between Σ^1 and Σ^3 bands. Additionally, the two possible final-state bands with dominant Σ^1-spatial symmetry (shifted down by 23.8 eV photon energy) are represented by the dash-dotted line for low damping and the dashed line for high damping within the solid.

Table II summarizes energy levels and splittings from Fig. 2 at high symmetry points of the Brillouin zone in comparison with other calculations and with experiment. The nonrelativistic band structure of Ref. 36 (last column) is very close to our original LMTO results (not shown), with minor differences attributable to the use of relativistic theory (Dirac equation) in our work. The exchange splitting is increased by about 0.2 eV to 2.17 eV (cf. first column) due to our energy-dependent real self-energy correction. Inclusion of the imaginary part, which accounts for the finite hole lifetime, slightly reduces it to 2.11 eV (cf. second column).

In view of interpreting our dichroic photoemission spectra, we added to Fig. 2 final-state bands with dominant Σ^1 symmetry (steep-dashed and dash-dotted lines), which were calculated with the complex optical potential. These bands have been shifted downward by 23.8 eV photon energy (because at this photon energy the maximum MLD is observed, see below) so that crossings with the occupied bands correspond to possible direct photoemission transitions from bulk initial states. For each relativistic representation there are two final-state bands. Our calculation shows that the corresponding states differ in their decay length along the [110]

TABLE II. Binding energies, exchange splittings, and spin-orbit splittings at Γ (in eV relative to E_F). Theoretical values from band structures (calculated with real potential) and from densities of states (calculated with potential including the imaginary part specified in Sec. III) are indicated by ''bands'' and ''DOS,'' respectively. The former are compared to results from Ref. 36. Energy levels are labeled by their single-group representations; $\langle\ \rangle$ denotes the mean value.

	This work			Ref. 36
	bands	DOS	Expt.	bands
Energy levels:				
$\Gamma^1=\langle\Gamma^1\uparrow\ \Gamma^1\downarrow\rangle$	9.56			8.24
$\Gamma^{25'}\uparrow$	2.47	2.40	2.4	2.26
$\Gamma^{12'}\uparrow$	0.99	0.95	0.9	0.94
$\Gamma^{25'}\downarrow$	0.30	0.29	0.3	0.34
$\Gamma^{12'}\downarrow$	−1.31			
Δ_{EXC}:				
$\Gamma^{25'}\downarrow-\Gamma^{25'}\uparrow$	2.17	2.11	2.1	1.92
Δ_{SOC}:				
$\Gamma^{25'}\uparrow$	0.07			
$\Gamma^{25'}\downarrow$	0.057			

direction, i.e., in their penetration depth into the solid. The $1/e$ penetration depth of the final states of the dash-dotted band is larger than $10\ a_\perp/\pi$, whereas the one for the dashed band is smaller than $2\ a_\perp/\pi$.

B. Photoemission spectra

Results of our photoemission experiments and our corresponding calculations—obtained as specified in Secs. II and III B—are shown in Fig. 3 for a sequence of photon energies (as indicated) and both magnetization directions (solid and dotted curves). The experimental data are normalized to equal photon flux, i.e., plotted on the same intensity scale. The theoretical spectra have been multiplied by the Fermi function, folded by a Gaussian function corresponding to the experimental energy resolution and scaled such as to match the experimental S^{MLD} leading peak at 23.8 eV photon energy. Therefore, experimental and calculated spectra can directly be compared, bearing in mind the following differences. In the calculations, we used completely linearly polarized light and ''perfect'' angle resolution. Furthermore, the theoretical spectra are for zero temperature and do not contain an inelastic background.

We first establish that the peaks in the theoretical spectra, which were obtained within a one-step-model approach to photoemission, can be interpreted in terms of direct interband transitions from the initial-state bands shown in Fig. 2, if one takes into account the slight shift of the photoemission peaks to lower binding energies due to the imaginary potential describing the finite hole lifetime. For 23.8 eV photon energy, such transitions can be expected at energies where the final-state bands in Fig. 2 cross with initial-state bands of spatial symmetry character Σ^1 and Σ^3.

Since the final states belonging to the dash-dotted bands have an averaged six-times larger penetration depth into the solid than those belonging to the dashed bands, they should

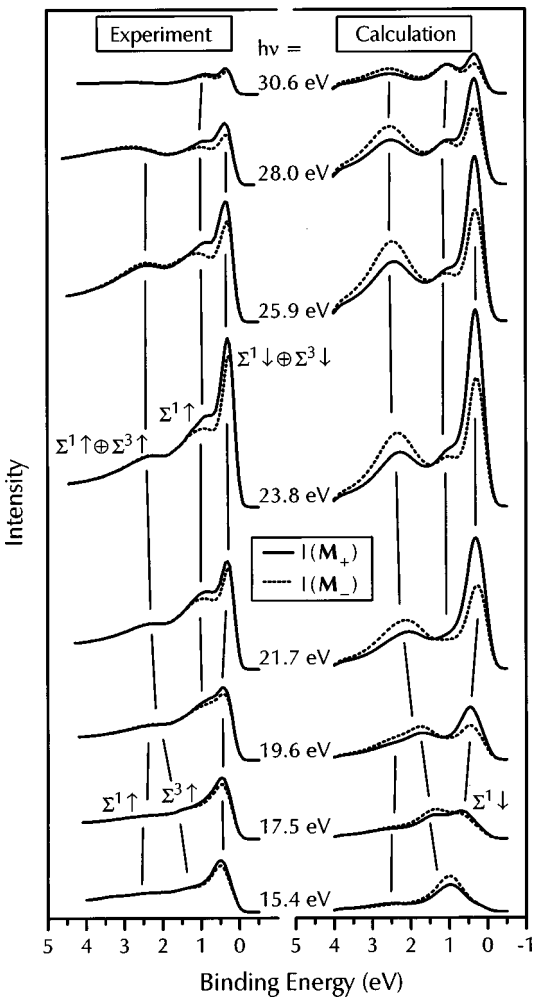

FIG. 3. Experimental (left panel) and calculated (right panel) photoemission intensities $I(\vec{M}_+)$ (solid line) and $I(\vec{M}_-)$ (dotted line) of Fe(110) for various photon energies $h\nu$. Vertical lines sketch the dispersion of the corresponding initial state. The labels give the spatial-spin symmetry of the dominating component of the respective initial state. The $\oplus$ denotes an incoherent superposition of the two initial states.

dominate the interpretation. This leaves us with five crossing points: (i) with the $\Sigma^1\uparrow$ band at 2.5 eV, (ii) with the $\Sigma^3\uparrow$ band at 2.3 eV, (iii) with the $\Sigma^1\uparrow$ band at 1 eV, (iv) with the $\Sigma^1\downarrow$ band at 0.3 eV, and (v) with the $\Sigma^3\downarrow$ band at 0.25 eV.

Since the spacing of points (i) and (ii) is less than the imaginary potential part (and of the order of the experimental energy resolution taken into account in the calculated spectra), the two transitions cannot be resolved, and in fact manifest themselves as a broad peak near 2.4 eV (for each magnetization direction) in the spectra in Fig. 3. With respect to nonrelativistic spatial-spin symmetry of the initial states this peak is labeled by $\Sigma^1\uparrow\oplus\Sigma^3\uparrow$. (The $\oplus$ denotes the incoherent superposition of the two transitions that cannot be resolved due to the limited energy resolution.) Crossing point (iii) corresponds to the photoemission peak $\Sigma^1\uparrow$ at 0.9 eV in Fig. 3. Transitions pertaining to (iv) and (v) are merged due to the experimental energy resolution and show up as the dominant peak $\Sigma^1\downarrow\oplus\Sigma^3\downarrow$ at 0.3 eV. The above discussion extends analogously to the other photon energies. The changes of

peak energies with photon energy, which reflect the dispersions of these bands, are sketched by the solid vertical lines in Fig. 3.

We now proceed to a more detailed discussion. The structure $\Sigma^1\uparrow\oplus\Sigma^3\uparrow$ shows no significant dispersion above 22 eV photon energy. Below 22 eV it splits into the two peaks $\Sigma^3\uparrow$ and $\Sigma^1\uparrow$ following the upwards dispersion of the Σ^3 and the nearly constant binding energy of the Σ^1 band. The transition at $\Gamma^{25'}\uparrow$ is reached at 29 eV photon energy (obtained by further downshifting the final-state dispersion). Dispersion and peak form are well described by the calculation, but it overrates the intensities of the $\Sigma^1\uparrow\oplus\Sigma^3\uparrow$ structure. The intensity is determined by the transition-matrix elements as well as self-energy corrections that are nonlocal and depend on the binding energy. In our calculations we assume a spatially constant self-energy and a linear dependence on the energy (cf. Sec. III B). Thus this deviation can be explained by the breakdown of the linear approximation at these binding energies.

The corresponding exchange-split γ_- states give rise to the big $\Sigma^1\downarrow\oplus\Sigma^3\downarrow$ feature close to the Fermi level. For photon energies below 21 eV, the $\Sigma^3\downarrow$ disperses above E_F. Both in the experimental and the theoretical spectra, one observes with decreasing photon energy only the dispersion of $\Sigma^1\downarrow$ to higher binding energies, a decrease of the intensity and a broadening of the peak form. With increasing photon energy, the $\Gamma^{25'}\downarrow$ point is reached at 26.8 eV.

Emission from the $\Sigma^2\uparrow$ and the $\Sigma^2\downarrow$ band, which near Γ might add to the $\Sigma^1\uparrow\oplus\Sigma^3\uparrow$ and the $\Sigma^1\downarrow\oplus\Sigma^3\downarrow$ peak, respectively, is negligible, because first, spatial symmetry Σ^2 parts cannot contribute to the transition-matrix elements in normal emission, and second, the Σ^1 and Σ^3 admixtures, which can contribute, are very small.

Around 0.9 eV binding energy, the $\Sigma^1\uparrow$ peak appears, for which the transition at $\Gamma^{12}\uparrow$ takes place at 27.25 eV photon energy. While experiment and theory agree in the binding energy of this peak, its intensity is much larger in the experimental than in the calculated spectra. In search for an explanation, we turn to the γ_- band with dominant $\Sigma^4\uparrow$ symmetry. For purely p-polarized light incident in the [001] azimuth, this band yields hardly any emission, since matrix element parts with Σ^4 states vanish and Σ^1 and Σ^3 admixtures are very small. For s-polarized light, however, Σ^4-derived emission is quite sizable. Since the light used in our experiment is not completely p polarized, i.e., contains an s-polarized component, the measured peak near 0.9 eV may have an additional Σ^4-derived contribution, which is absent in its theoretical counterpart.

For the critical points of the quasiparticle band structure, experimental binding energies have been obtained by fitting the measured S^{MLD} by Gaussians after subtraction of a Shirley-like background for the corresponding photon energy for which the transitions take place at Γ. These values and the exchange splitting are seen, in Table II, to agree excellently with their calculated quasiparticle counterparts (in the column ''DOS''). The deviations from the results of the ground-state band structure of Ref. 36, which are very close to our own LMTO ground-state band structure, clearly demonstrate that a real and an imaginary self-energy correction as specified in Sec. III is significant. The comparison of earlier experimental binding energies for Fe(110) with various ground-state calculation results, which has been shown in Table II of Ref. 37, further supports this finding. For a more detailed discussion on self-energy corrections in photoemission from Fe—as obtained for Fe(001)—we refer to Refs. 38 and 39.

C. Magnetic linear dichroism

We now turn to the MLD. Figure 3 reveals that for various photon energies the two spectra $I(\vec{M}_+)$ and $I(\vec{M}_-)$ measured for the two different orientations of the magnetization along [110] are different. Hence, a magnetic dichroism is observed and D^{MLD} is unequal zero.

In detail, the $\Sigma^1\uparrow\oplus\Sigma^3\uparrow$ transition possesses a negative difference D^{MLD}, i.e., the $I(\vec{M}_-)$ intensity exceeds the $I(\vec{M}_+)$ one. Its calculated MLD exists in the whole investigated photon-energy range with a pronounced maximum at around 23 eV, whereas the experimental MLD is significantly nonzero only from approximately 24 eV up to 29 eV with its maximum at 26 eV. For the $\Sigma^1\downarrow\oplus\Sigma^3\downarrow$ structure a positive MLD is observed in both the experimental and theoretical spectra in the whole photon-energy range. For excitations below 21 eV, the photoemission calculations with a very small imaginary part of the self-energy (not shown here) reveal that both Σ states contribute to the MLD with the same sign.

We now address the question of whether the analytical theory sketched in Sec. III A is capable of explaining the observed MLD. As a first step, one has to identify those initial states within the Brillouin zone from which MLD is expected. Referring to the theory, these are states significantly hybridized by SOC, i.e., states near SOC-induced band gaps where hybridization is strongest. In our geometry the relevant anticrossing points are between nonrelativistic Σ^1 and Σ^3 bands with the same spin, i.e., the points A and B at the Γ point and the points C and D in the middle of the Brillouin zone (cf. Fig. 2).

As a second step, one has to show that MLD is observed if the corresponding direct transitions are near such anticrossing points. This statement will be discussed for the example of the prominent $\Sigma^1\downarrow\oplus\Sigma^3\downarrow$ structure for which the dependence of S^{MLD} and D^{MLD} on the photon energy is given in Fig. 4. A comparison of experiment with theory is facilitated for this structure by the low background of secondary electrons for transitions directly below E_F. D^{MLD} and S^{MLD} have been obtained from the intensities $I(\vec{M}_+)$ and $I(\vec{M}_-)$ at the respective peak position. Some remarks on the errors in Fig. 4 should be made. The statistical error in the intensity and the systematical one in the photon energy is within the symbol size. Due to the strong dependence of S^{MLD}, and especially of D^{MLD} on the binding energy, the systematical error in S^{MLD} and D^{MLD} is larger and can be approximated by the scattering of the points. The scaling between calculation and experiment is the same as in Fig. 3; experimental and calculated S^{MLD} at 23.8 eV photon energy have the same height. Therefore S^{MLD} and D^{MLD} can directly be compared to the experimental data. Note that the difference D^{MLD} has been plotted on a five-times larger scale

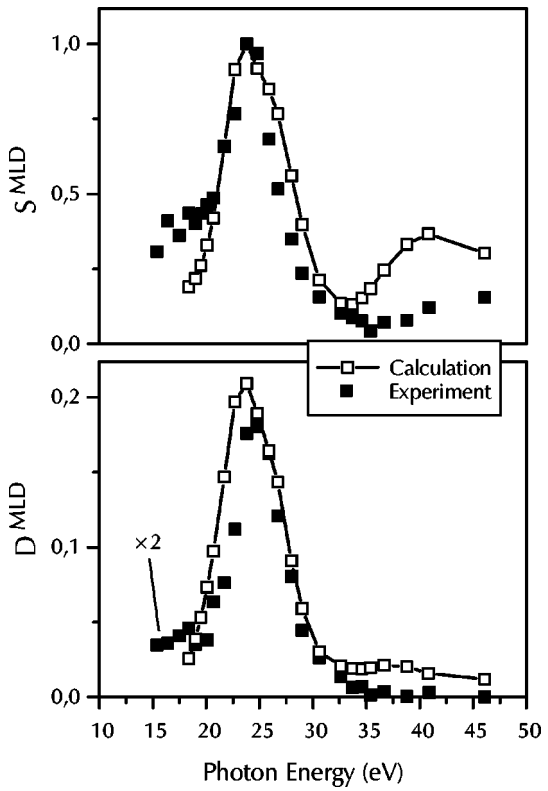

FIG. 4. Photon-energy dependence of sum S^{MLD} (upper panel) and difference D^{MLD} (lower panel) of the $\Sigma^1\downarrow \oplus\ \Sigma^3\downarrow$ structure. Experimental and calculated S^{MLD} are scaled to have the same height at 23.8 eV, D^{MLD} is plotted on a fivefold larger scale. Within this scale the experimental D^{MLD} has been multiplied by a factor of 2.

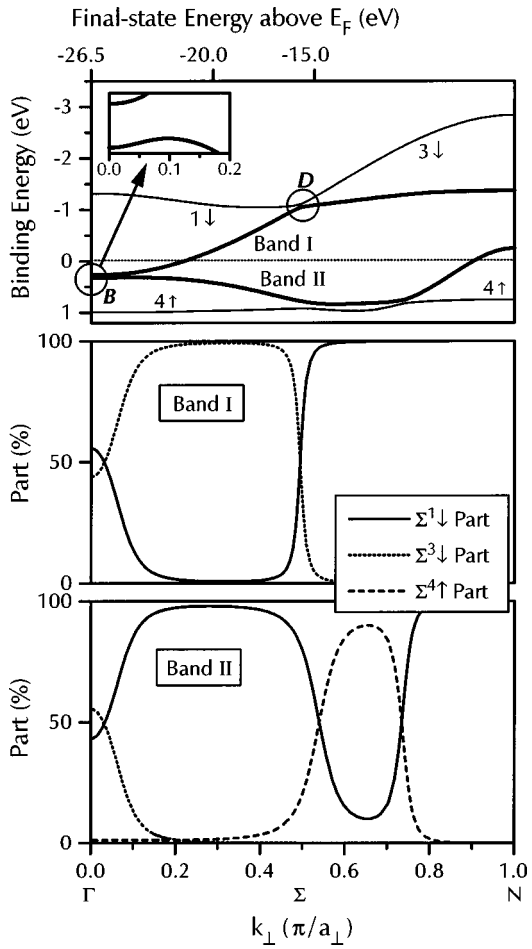

FIG. 5. Detailed dispersion of the initial states of the $\Sigma^1\downarrow \oplus \Sigma^3\downarrow$ structure labeled by bands *I* and *II* represented in the upper panel and in the inset by thick lines. Dependence of the $\Sigma^1\downarrow$ and $\Sigma^3\downarrow$ parts of band *I* (middle panel) and of the $\Sigma^1\downarrow$, $\Sigma^3\downarrow$, and $\Sigma^1\downarrow$ parts of band *II* (lower panel) on $k_\perp$ and the final-state energy above E_{F}.

in comparison to S^{MLD}. Within this scale the measured D^{MLD} has been multiplied by a factor of 2 to fit approximately the calculated one.

We find a good qualitative agreement between experiment and calculation of S^{MLD} and D^{MLD} regarding the photon-energy dependence below 31 eV. Both quantities exhibit a pronounced maximum at around 24 eV. For photon energies above 33 eV the calculated S^{MLD} differs from the measured one by a second weaker maximum at around 40 eV. For D^{MLD} the agreement above 33 eV is much better; in both experiment and calculation a decreasing MLD difference is observed.

In order to explain the dependence of S^{MLD} and D^{MLD} on the photon energy, we have additionally projected out the parts of $\Sigma^1\downarrow$ and $\Sigma^3\downarrow$ functions of each of the two relevant initial-state bands. The result is shown in the middle and lower panels of Fig. 5 as a function of $k_\perp$. In addition, the final-state energy is given in the upper horizontal scale of Fig. 5. This scale is based on the corresponding direct transition into that final state with practically no damping (dash-dotted line in Fig. 2). Above -27 eV binding energy, both final states contribute approximately equally to the photoemission spectra due to their comparable damping. The upper panel of Fig. 5 repeats the relevant part of the band structure. The two initial states are represented by bold lines and labeled as bands *I* and *II*. The inset shows the detailed band structure near the Γ point.

Figure 5 reveals that the bands change their character due to hybridization; both bands at band gap *B* and additionally band *I* at point *D* and band *II* at the two anticrossing points with the flat $\Sigma^4\uparrow$ band at about 1 eV binding energy. Note that due to the complicated dispersion at *B* (cf. the inset in Fig. 5) the maximum degree of hybridization between $\Sigma^1\downarrow$ and $\Sigma^3\downarrow$ for the two bands are at $k_\perp = 0.03\pi/a_\perp$ and not directly at $\Gamma(k_\perp = 0)$.

We now return to the discussion and show how the photon-energy dependence of the $\Sigma^1\downarrow\oplus\Sigma^3\downarrow$ MLD can be explained by the band structure and hybridization at point *B*. At around 15 eV photon energy, the transitions take place nearly in the middle of the Brillouin zone. Up to 21 eV, only transitions from the initial-state band *II* are observed with a broad peak below E_{F} in the photoemission spectra. At the corresponding $\vec{k}$ points the initial state consists of a hybrid of $\Sigma^1\downarrow$ and $\Sigma^4\uparrow$ functions (cf. Fig. 5, lower panel) so that, if the model is correct, no MLD should be observed. In fact a small and nearly constant experimental D^{MLD} is observed, caused by the breakdown of the direct-transition picture into one final state.

Above 21 eV, band-*I*-derived transitions are possible. In the photoemission spectra the prominent structure $\Sigma^1\downarrow$

$\oplus\Sigma^3\downarrow$ occurs and therefore S^{MLD} increases with a maximum at 23.8 eV. Additionally, the increase of D^{MLD} is observed. Within our model this can easily be explained by the increasing hybridization of the initial states near band gap B. The maximum of D^{MLD} is reached at 24.8 eV or $k_\perp = 0.05\pi/a_\perp$, which is nearly exact at the maximum degree of hybridization of the two bands at $k_\perp = 0.03\pi/a_\perp$. Above 25 eV, S^{MLD} decreases, i.e., the transition-matrix elements become smaller. Therefore, D^{MLD}, which depends linearly on the matrix elements, decreases. Note that the above interpretation assumes that the transition-matrix elements vary slowly with photon energy.

The above comparison between the photon-energy dependence of D^{MLD} with the initial-state dispersion shows that the $\Sigma^1\downarrow\oplus\Sigma^3\downarrow$ MLD can be explained by the dispersion and the hybridization of the corresponding initial states of bands I and II. We want to emphasize at this point that the MLD is not caused by incoherent superposition of the transitions from the two individual initial states that would lead to a vanishing D^{MLD}. In fact, MLD is an interference effect caused by the coherent excitation of a $\Sigma^1\downarrow$- and a $\Sigma^3\downarrow$-related part from each of the two initial states.

In the same way the MLD of the exchange-split $\Sigma^1\uparrow\oplus\Sigma^3\uparrow$ structure can be explained by the hybridization at the SOC-induced band gap A. Additionally, within the analytical framework, it is easy to explain the opposite signs of the $\Sigma^1\uparrow\oplus\Sigma^3\uparrow$ and $\Sigma^1\downarrow\oplus\Sigma^3\downarrow$ structures. Basing on nearly the same dispersion near Γ of the $\Sigma^1\uparrow$ and $\Sigma^3\uparrow$ initial states on the one side and the $\Sigma^1\downarrow$ and $\Sigma^3\downarrow$ initial states on the other side, it is a good assumption that the corresponding transition-matrix elements are comparable. But, as can be seen in Eq. (2), the interference terms of the exchange-split states γ_+ and γ_- possess opposite signs in D^{MLD}. Hence, if now the matrix elements are independent of the photon energy, especially the phase difference between the two partial waves, the sign reversal is observed.

In the experimental spectra the $\Sigma^1\uparrow$ transition at 0.9 eV also seems to have a MLD for photon energies larger than 19.6 eV. But in our interpretation its MLD can be explained by an artifact caused by the rather small energy separation of about 0.7 eV from the $\Sigma^1\downarrow\oplus\Sigma^3\downarrow$ structure and its dominating positive MLD. This interpretation is proven first by the fact that in the experimental 25.9 eV spectra the MLD reverses sign at the $\Sigma^1\uparrow$ peak position and, second, by fitting the individual peaks of the experimental spectra for both magnetization directions (after subtracting a Shirley-like background). In addition, in the calculated spectra this peak shows no MLD.

This observation is expected within the direct-transition picture combined with hybridization analysis. Transitions near C are possible at photon energies around 16 eV. But for these photon energies the $\Sigma^1\uparrow$ emission near 0.9 eV decreases as can be seen in Fig. 3, i.e., corresponding matrix elements and hence the interference terms become small. For higher photon energies the emission from the $\Sigma^1\uparrow$ band increases but possible $\Sigma^3\uparrow$ admixtures are negligible due to the large energy separation in comparison to the exchange splitting from the downwards dispersing $\Sigma^3\uparrow$ band (cf. Fig. 2). Hence, no MLD is observed.

Point D belongs to the unoccupied band structure and cannot be observed in the experimental photoemission spectra. But calculated (inverse photoemission) spectra that include transitions from initial states above E_{F} also show MLD at this point.

In summary, the MLD of photoemission calculations and of measurements can qualitatively be explained by the analytical theory in combination with the band structure accompanied by hybridization analysis. Differences between analytical theory and measurements as well as calculations can be attributed to simplifications in the above discussion, for example, the neglect of the dependence of E', ϑ', and the phase difference between the two partial waves on photon energy and the restriction to one direct transition.

In the following we now want to discuss the discrepancies between photoemission calculations and measurements: (i) For photon energies above 31 eV the calculated intensity S^{MLD} increases, whereas the experimental one is almost independent of the photon energy. As mentioned above, the photoemission intensity is additionally determined by self-energy corrections. Thus the different dependence of S^{MLD} on the photon energy can be attributed to the self-energy corrections in the upper state regime that cannot be described by our linear approximation (cf. Sec. III B).

(ii) The calculations overrate the MLD approximately by a factor of 2 in the whole investigated photon-energy range under the assumption that experimental and calculated S^{MLD} at 23.8 eV have the same value. The overrating of the MLD has two possible reasons; first, the calculations have been done under ''perfect conditions,'' i.e., with fully linearly polarized light and the magnetization at zero temperature. Therefore, the calculated MLD should exceed the experimental one. Additionally, effects of spin-dependent and inelastic scattering as well as a spin-dependent lifetime have not been incorporated in the calculations. This could lead to a decrease of the dichroism. For the same reason it is possible that the experimental D^{MLD} of the $\Sigma^1\uparrow\oplus\Sigma^3\uparrow$ structure is smaller in comparison to the $\Sigma^1\downarrow\oplus\Sigma^3\downarrow$ MLD. Second, as an interference effect the MLD should be very sensitive to experimental conditions as well as numerical modeling. From the experimental point of view these are the preparation conditions and possible contamination at the surface that can influence the MLD. (An effect of contamination in our experiment can be neglected, since it was checked by repeated measurements of the MLD after several hours.)

Based on these results, we can offer a few comments on the question of how MLD in the valence-band photoemission can be used to obtain further information on the magnetic ground state of the system, such as spin and orbital magnetic moments. Because MLD depends strongly on the detailed electronic structure, this seems to be hardly possible. For example, if the phase difference between the two partial waves $\Delta\mu$ satisfies $\mathrm{Im}[\sin\vartheta'\cos\vartheta'^{\star}\exp(\Delta\mu)]=0$, no MLD is observed. Furthermore, MLD depends on the absolute value of the involved matrix elements. So that, if the transition is forbidden due to the selection rule $\Delta l=\pm 1$, again no MLD is observed. This may be the reason why different MLDs are observed for the same initial state. In our case, for example, the transitions of $\Sigma^1\downarrow\oplus\Sigma^3\downarrow$ at 24 and 29 eV photon energy into the same final state start at the same initial states of band I and II. But both exhibit different D^{MLD},

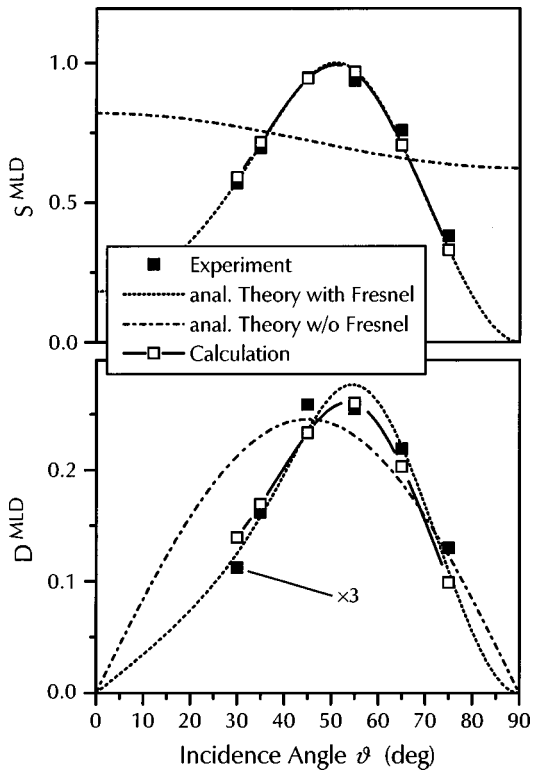

FIG. 6. Dependence on the angle of the impinging light for S^{MLD} (upper panel) and D^{MLD} (lower panel) of the $\Sigma^1\downarrow\oplus\Sigma^3\downarrow$ structure at 25.9 eV photon energy. Additionally, two fits are given based on the analytical theory with (dotted line) and without (dash-dotted line) optical response. Experimental and calculated S^{MLD} are scaled to have the same height, D^{MLD} is plotted on a fourfold larger scale. Within this scale the experimental D^{MLD} has been multiplied by a factor of 3.

which can easily be explained by the different absolute values of matrix elements. This may be called a *final-state effect* because the initial-state wave functions are the same at both photon energies.

The detailed analysis above shows a delicate behavior of MLD on both exchange splitting and SOC. Thus, a simple rule of thumb, for example, that magnetic dichroism depends linearly on the magnetization and therefore can be regarded as a measure for the latter, can hardly be true, in particular in valence-band photoemission. Such information can possibly be derived by comparing the measurements with fully relativistic photoemission and band-structure calculations.

D. Dependence on light incidence angle

Correctness and relevance of both the analytical and numerical calculations can directly be proven by comparing the experimental and the theoretical dependence of S^{MLD} and D^{MLD} on the polar angle of incidence ϑ of the light. To verify the theoretical predictions, S^{MLD} and D^{MLD} of the $\Sigma^1\downarrow\oplus\Sigma^3\downarrow$ structure at 25.9 eV photon energy (0.4 eV binding energy) have been recorded experimentally for various polar angles ϑ. The result is represented by the solid squares in Fig. 6. For the errors the same argumentation holds as in Fig. 4.

The numerical data (open squares with solid lines) have been obtained from photoemission calculations. These have been scaled by a common factor in order to best fit the experimental S^{MLD}. At this photon energy the numerical D^{MLD} overrates the experimental one by a factor of 3, which has been incorporated in the lower panel of Fig. 6.

Within the external field approximation, i.e., without Snell's law and Fresnel's formula (dash-dotted lines in Fig. 6), the analytical formula predicts a $\sin 2\vartheta$ dependence of D^{MLD} and a superposition of $\sin^2\vartheta$ and $\cos^2\vartheta$ dependences of S^{MLD}. The result of a fit to D^{MLD} based on this approximation is additionally shown. The discrepancy between both experimental and calculated S^{MLD} and D^{MLD} completely rules out the external field approximation. Thus, the refraction of the light has to be incorporated.

The analytical results with optical response of the metal (dotted lines in Fig. 6) were obtained from Eq. (2) by fitting simultaneously S^{MLD} and D^{MLD} and using Snell's law and Fresnels' formula, regarding the transition-matrix elements as parameters. For the complex index of refraction we took $\epsilon = 0.54 + 0.31\mathrm{i}$ (as in the photoemission calculations) from Ref. 40. We assumed two initial states, i.e., the bands with nonrelativistic $\Sigma^1\downarrow$ and $\Sigma^3\downarrow$ symmetry, both with three independent parameters; the absolute values $|M^{(1fi)}|$ and $|M^{(3fi)}|$ of the transition-matrix elements and the phase difference between them.

The experimental as well as the numerical data are well reproduced by the analytical fit. This proves clearly that MLD is described correctly by our analytical theory, especially by Eq. (2). The good agreement for D^{MLD} is only achieved if one assumes two initial states. Thus, one can conclude about the number of initial states for the $\Sigma^1\downarrow\oplus\Sigma^1\downarrow$ structure by measuring the incidence-angle dependence of D^{MLD}.

Additionally, one concludes that the angular dependence of the MLD observed in the valence-band structure of Fe(110) is properly described by classical Fresnel theory. At first glance, it seems surprising that the optical response in the topmost surface layers can be neglected in the interpretation of photoemission spectra from Fe(110) in the VUV energy range, contrary to findings for layered semiconductors.[41] The next step beyond the Fresnel approximation, the so-called hydrodynamical model,[42] leads to longitudinal electromagnetic partial waves, which in spin-polarized photoemission from Pt(001) can be completely neglected due to the very low effective plasmon energy with respect to the photon energy.[28] The latter result may be regarded as valid also for Fe(110).

In principle, referring to the incidence angle dependence of the MLD, it is possible to calculate the *absolute* values of the photoemission transitions and the phase difference between them. Unfortunately, in our case this is not possible because the corresponding peak is a superposition of two maxima and, therefore, the fit is not unambiguous. However, in the bare calculated spectra (without folding with the experimental resolution) the initial states can be separated.

V. CONCLUSION

We have presented an investigation of MLD in valence-band photoemission from Fe(110) in a fourfold way: by symmetry considerations, analytical theory, numerical calculations, and measurements. We have shown that by comparing

experimental and theoretical results the microscopic origin of MLD is mainly the SOC-induced hybridization of the initial states. If the various components of such a hybrid are simultaneously excited, one observes an interference between the partial waves. The sign of the interference term depends on the magnetization direction and thus MLD is observed. The agreement of the experimental results with both the predictions of the analytical formula and the quantitative results of the numerical calculations proves that our theoretical description of MLD is adequate. Other models, if properly enhanced, for example, by relativistic group theory and relativistic photoemission theory, should also lead to the same conclusions.[13–15] In summary, one can use MLD to identify SOC-induced band gaps or hybridization zones in the band structure by measuring the photon-energy dependence of D^{MLD}.

For the case of Fe(110) on W(110), we have further shown that the observed MLD is derived from the SOC-induced gaps at $\Gamma^{25'}\uparrow$ and $\Gamma^{25'}\downarrow$ and that the MLD signals of the exchange-split states possess opposite sign. The photon-energy dependence of the $\Gamma^{25'}\downarrow$-related MLD can be explained by means of the initial-state band structure of bulk Fe(110) within the direct-transition picture. Furthermore, theory reveals a substantial influence of the refraction of the incident radiation on the MLD, and comparison with experiment shows that a description of the radiation field inside the metal in terms of classical Fresnel optics is adequate for photon energies in the VUV regime.

ACKNOWLEDGMENTS

We thank M. Mast and W. Braun for their help during the measurements at BESSY, Berlin. The experiments have been supported by the Bundesministerium für Bildung, Wissenschaft, Forschung und Technologie (BMBF) under Contract No. 05 5PCFXB 2 and by the Deutsche Forschungsgemeinschaft through SFB 341. The theoretical work has been financially supported by the BMBF under Contract No. 05 621PGA.

[1] G. Schütz, W. Wagner, W. Wilhelm, P. Kienle, R. Zeller, R. Frahm, and G. Materlik, Phys. Rev. Lett. **58**, 737 (1987).
[2] L. Baumgarten, C. M. Schneider, H. Petersen, F. Schäfers, and J. Kirschner, Phys. Rev. Lett. **65**, 492 (1990).
[3] C. M. Schneider, M. S. Hammond, P. Schuster, A. Cebollada, R. Miranda, and J. Kirschner, Phys. Rev. B **44**, 12 066 (1991).
[4] H. B. Rose, C. Roth, F. U. Hillebrecht, and E. Kisker, Solid State Commun. **91**, 129 (1994).
[5] C. Roth, F. U. Hillebrecht, H. B. Rose, and E. Kisker, Phys. Rev. Lett. **70**, 3479 (1993).
[6] M. Getzlaff, C. Ostertag, G. H. Fecher, N. A. Cherepkov, and G. Schönhense, Phys. Rev. Lett. **73**, 3030 (1994).
[7] B. T. Thole and G. van der Laan, Phys. Rev. B **44**, 12 424 (1991).
[8] G. van der Laan, Phys. Rev. B **51**, 240 (1995).
[9] D. Venus, Phys. Rev. B **48**, 6144 (1993).
[10] T. Scheunemann, S. Halilov, J. Henk, and R. Feder, Solid State Commun. **91**, 487 (1994).
[11] J. Henk, S. Halilov, T. Scheunemann, and R. Feder, Phys. Rev. B **50**, 8130 (1994).
[12] J. Henk, T. Scheunemann, S. Halilov, and R. Feder, J. Phys.: Condens. Matter **8**, 47 (1996).
[13] D. Venus, Phys. Rev. B **49**, 8821 (1994).
[14] D. Venus, J. Magn. Magn. Mater. **170**, 29 (1997).
[15] D. Venus, Phys. Rev. B **56**, 2661 (1997).
[16] *Spin-Orbit Influenced Spectroscopies of Magnetic Solids*, Vol. 466 of Lecture Notes in Physics, edited by H. Ebert and G. Schütz (Springer, Berlin, 1996).
[17] W. Kuch, A. Dittschar, K. Meinel, M. Zharnikov, C. Schneider, J. Kirschner, J. Henk, and R. Feder, Phys. Rev. B **53**, 11 621 (1996).
[18] J. Henk and R. Feder, Phys. Rev. B **55**, 11 476 (1997).
[19] A. Fanelsa, E. Kisker, J. Henk, and R. Feder, Phys. Rev. B **54**, 2922 (1996).
[20] W. Kuch, A. Dittschar, M.-T. Lin, M. Salvietti, M. Zharnikov, C. M. Schneider, J. Kirschner, J. Camamero, and J. J. de Miguel, J. Magn. Magn. Mater. **170**, L13 (1997).
[21] U. Gradmann and G. Waller, Surf. Sci. **116**, 539 (1982); H. J. Elmers and U. Gradmann, Appl. Phys. A: Solids Surf. **51**, 255 (1990); H. Bethge, D. Heuer, C. Jensen, K. Reshöft, and U. Köhler, Surf. Sci. **331-333**, 878 (1995).
[22] T. Inui, Y. Tanabe, and Y. Onodera, in *Group Theory and Its Applications in Physics*, Vol. 78 of *Springer Series in Solid State Sciences*, edited by M. Cardona (Springer, Berlin, 1990).
[23] L. Falicov and J. Ruvalds, Phys. Rev. **172**, 498 (1968).
[24] E. Tamura and R. Feder, Solid State Commun. **79**, 989 (1991).
[25] E. Tamura and R. Feder, Europhys. Lett. **16**, 695 (1991).
[26] J. Hermanson, Solid State Commun. **22**, 9 (1977).
[27] J. D. Jackson, *Classical Electrodynamics* (Wiley, New York, 1975).
[28] J. Henk, T. Scheunemann, and R. Feder, J. Phys.: Condens. Matter **9**, 2963 (1997).
[29] B. Schmiedeskamp, N. Irmer, R. David, and U. Heinzmann, Appl. Phys. A: Solids Surf. **53**, 418 (1991).
[30] R. Feder and J. Henk, in Ref. 16.
[31] *Polarized Electrons in Surface Physics*, edited by R. Feder, Advanced Series in Surface Science (World Scientific, Singapore, 1985).
[32] *Electron Scattering Theory of Ordered and Disordered Matter*, edited by P. Weinberger (Clarendon, Oxford, 1990).
[33] E. Tamura, R. Feder, G. Waller, and U. Gradmann, Phys. Lett. B **157**, 627 (1990).
[34] J. W. Krewer and R. Feder, Phys. Lett. B **172**, 135 (1991).
[35] R. Wu and A. Freeman, Phys. Rev. Lett. **69**, 2867 (1992).
[36] K. Hathaway, H. Jansen, and A. Freeman, Phys. Rev. B **31**, 7603 (1985).
[37] A. M. Turner, A. W. Donoho, and J. L. Erskine, Phys. Rev. B **29**, 2986 (1984).
[38] R. Feder, A. Rodriguez, U. Baier, and E. Kisker, Solid State Commun. **52**, 57 (1984).
[39] R. Clauberg and R. Feder, in *Polarized Electrons in Surface*

Physics, (Ref. 31), Chap. 14, p. 565.
[40] H. Hagemann, W. Gudat, and C. Kunz, Technical Report No. SR-74/7, Deutsches Elektronen-Synchrotron Hamburg (unpublished).
[41] D. Samuelsen, A. Yang, and W. Schattke, Surf. Sci. **287**, 676 (1993).
[42] F. Forstmann and R. Gerhardts, *Metal Optics Near the Plasma Frequency* (Springer, Berlin, 1986).